

# First Measurement of $Z/\gamma^*$ Production in Compton Scattering of Quasi-real Photons

The OPAL Collaboration

## Abstract

We report the first observation of  $Z/\gamma^*$  production in Compton scattering of quasi-real photons. This is a subprocess of the reaction  $e^+e^- \rightarrow e^+e^-Z/\gamma^*$ , where one of the final state electrons is undetected. Approximately  $55 \text{ pb}^{-1}$  of data collected in the year 1997 at an  $e^+e^-$  centre-of-mass energy of 183 GeV with the OPAL detector at LEP have been analysed. The  $Z/\gamma^*$  from Compton scattering has been detected in the hadronic decay channel. Within well defined kinematic bounds, we measure the product of cross-section and  $Z/\gamma^*$  branching ratio to hadrons to be  $(0.9 \pm 0.3 \pm 0.1) \text{ pb}$  for events with a hadronic mass larger than 60 GeV, dominated by  $(e)eZ$  production. In the hadronic mass region between 5 GeV and 60 GeV, dominated by  $(e)e\gamma^*$  production, this product is found to be  $(4.1 \pm 1.6 \pm 0.6) \text{ pb}$ . Our results agree with the predictions of two Monte Carlo event generators, grc4f and PYTHIA.

(Submitted to Physics Letters B)

# The OPAL Collaboration

G. Abbiendi<sup>2</sup>, K. Ackerstaff<sup>8</sup>, G. Alexander<sup>23</sup>, J. Allison<sup>16</sup>, N. Altekamp<sup>5</sup>, K.J. Anderson<sup>9</sup>, S. Anderson<sup>12</sup>, S. Arcelli<sup>17</sup>, S. Asai<sup>24</sup>, S.F. Ashby<sup>1</sup>, D. Axen<sup>29</sup>, G. Azuelos<sup>18,a</sup>, A.H. Ball<sup>17</sup>, E. Barberio<sup>8</sup>, R.J. Barlow<sup>16</sup>, R. Bartoldus<sup>3</sup>, J.R. Batley<sup>5</sup>, S. Baumann<sup>3</sup>, J. Bechtluft<sup>14</sup>, T. Behnke<sup>27</sup>, K.W. Bell<sup>20</sup>, G. Bella<sup>23</sup>, A. Bellerive<sup>9</sup>, S. Bentvelsen<sup>8</sup>, S. Bethke<sup>14</sup>, S. Betts<sup>15</sup>, O. Biebel<sup>14</sup>, A. Biguzzi<sup>5</sup>, S.D. Bird<sup>16</sup>, V. Blobel<sup>27</sup>, I.J. Bloodworth<sup>1</sup>, M. Bobinski<sup>10</sup>, P. Bock<sup>11</sup>, J. Böhme<sup>14</sup>, D. Bonacorsi<sup>2</sup>, M. Boutemour<sup>34</sup>, S. Braibant<sup>8</sup>, P. Bright-Thomas<sup>1</sup>, L. Brigliadori<sup>2</sup>, R.M. Brown<sup>20</sup>, H.J. Burckhart<sup>8</sup>, C. Burgard<sup>8</sup>, R. Bürgin<sup>10</sup>, P. Capiluppi<sup>2</sup>, R.K. Carnegie<sup>6</sup>, A.A. Carter<sup>13</sup>, J.R. Carter<sup>5</sup>, C.Y. Chang<sup>17</sup>, D.G. Charlton<sup>1,b</sup>, D. Chrisman<sup>4</sup>, C. Ciocca<sup>2</sup>, P.E.L. Clarke<sup>15</sup>, E. Clay<sup>15</sup>, I. Cohen<sup>23</sup>, J.E. Conboy<sup>15</sup>, O.C. Cooke<sup>8</sup>, C. Couyoumtzelis<sup>13</sup>, R.L. Coxe<sup>9</sup>, M. Cuffiani<sup>2</sup>, S. Dado<sup>22</sup>, G.M. Dallavalle<sup>2</sup>, R. Davis<sup>30</sup>, S. De Jong<sup>12</sup>, L.A. del Pozo<sup>4</sup>, A. de Roeck<sup>8</sup>, K. Desch<sup>8</sup>, B. Dienes<sup>33,d</sup>, M.S. Dixit<sup>7</sup>, J. Dubbert<sup>34</sup>, E. Duchovni<sup>26</sup>, G. Duckeck<sup>34</sup>, I.P. Duerdoth<sup>16</sup>, D. Eatough<sup>16</sup>, P.G. Estabrooks<sup>6</sup>, E. Etzion<sup>23</sup>, H.G. Evans<sup>9</sup>, F. Fabbri<sup>2</sup>, M. Fanti<sup>2</sup>, A.A. Faust<sup>30</sup>, F. Fiedler<sup>27</sup>, M. Fierro<sup>2</sup>, I. Fleck<sup>8</sup>, R. Folman<sup>26</sup>, A. Fürties<sup>8</sup>, D.I. Futyan<sup>16</sup>, P. Gagnon<sup>7</sup>, J.W. Gary<sup>4</sup>, J. Gascon<sup>18</sup>, S.M. Gascon-Shotkin<sup>17</sup>, G. Gaycken<sup>27</sup>, C. Geich-Gimbel<sup>3</sup>, G. Giacomelli<sup>2</sup>, P. Giacomelli<sup>2</sup>, V. Gibson<sup>5</sup>, W.R. Gibson<sup>13</sup>, D.M. Gingrich<sup>30,a</sup>, D. Glenzinski<sup>9</sup>, J. Goldberg<sup>22</sup>, W. Gorn<sup>4</sup>, C. Grandi<sup>2</sup>, E. Gross<sup>26</sup>, J. Grunhaus<sup>23</sup>, M. Gruwé<sup>27</sup>, G.G. Hanson<sup>12</sup>, M. Hansroul<sup>8</sup>, M. Hapke<sup>13</sup>, K. Harder<sup>27</sup>, C.K. Hargrove<sup>7</sup>, C. Hartmann<sup>3</sup>, M. Hauschild<sup>8</sup>, C.M. Hawkes<sup>5</sup>, R. Hawkings<sup>27</sup>, R.J. Hemingway<sup>6</sup>, M. Herndon<sup>17</sup>, G. Herten<sup>10</sup>, R.D. Heuer<sup>8</sup>, M.D. Hildreth<sup>8</sup>, J.C. Hill<sup>5</sup>, S.J. Hillier<sup>1</sup>, P.R. Hobson<sup>25</sup>, A. Hocker<sup>9</sup>, R.J. Homer<sup>1</sup>, A.K. Honma<sup>28,a</sup>, D. Horváth<sup>32,c</sup>, K.R. Hossain<sup>30</sup>, R. Howard<sup>29</sup>, P. Hüntemeyer<sup>27</sup>, P. Igo-Kemenes<sup>11</sup>, D.C. Imrie<sup>25</sup>, K. Ishii<sup>24</sup>, F.R. Jacob<sup>20</sup>, A. Jawahery<sup>17</sup>, H. Jeremie<sup>18</sup>, M. Jimack<sup>1</sup>, C.R. Jones<sup>5</sup>, P. Jovanovic<sup>1</sup>, T.R. Junk<sup>6</sup>, D. Karlen<sup>6</sup>, V. Kartvelishvili<sup>16</sup>, K. Kawagoe<sup>24</sup>, T. Kawamoto<sup>24</sup>, P.I. Kayal<sup>30</sup>, R.K. Keeler<sup>28</sup>, R.G. Kellogg<sup>17</sup>, B.W. Kennedy<sup>20</sup>, A. Klier<sup>26</sup>, S. Kluth<sup>8</sup>, T. Kobayashi<sup>24</sup>, M. Kobel<sup>3,e</sup>, D.S. Koetke<sup>6</sup>, T.P. Kokott<sup>3</sup>, M. Kolrep<sup>10</sup>, S. Komamiya<sup>24</sup>, R.V. Kowalewski<sup>28</sup>, T. Kress<sup>11</sup>, P. Krieger<sup>6</sup>, J. von Krogh<sup>11</sup>, T. Kuhl<sup>3</sup>, P. Kyberd<sup>13</sup>, G.D. Lafferty<sup>16</sup>, D. Lanske<sup>14</sup>, J. Lauber<sup>15</sup>, S.R. Lautenschlager<sup>31</sup>, I. Lawson<sup>28</sup>, J.G. Layter<sup>4</sup>, D. Lazic<sup>22</sup>, A.M. Lee<sup>31</sup>, D. Lellouch<sup>26</sup>, J. Letts<sup>12</sup>, L. Levinson<sup>26</sup>, R. Liebisch<sup>11</sup>, B. List<sup>8</sup>, C. Littlewood<sup>5</sup>, A.W. Lloyd<sup>1</sup>, S.L. Lloyd<sup>13</sup>, F.K. Loebinger<sup>16</sup>, G.D. Long<sup>28</sup>, M.J. Losty<sup>7</sup>, J. Ludwig<sup>10</sup>, D. Liu<sup>12</sup>, A. Macchiolo<sup>2</sup>, A. Macpherson<sup>30</sup>, W. Mader<sup>3</sup>, M. Mannelli<sup>8</sup>, S. Marcellini<sup>2</sup>, C. Markopoulos<sup>13</sup>, A.J. Martin<sup>13</sup>, J.P. Martin<sup>18</sup>, G. Martinez<sup>17</sup>, T. Mashimo<sup>24</sup>, P. Mättig<sup>26</sup>, W.J. McDonald<sup>30</sup>, J. McKenna<sup>29</sup>, E.A. Mckigney<sup>15</sup>, T.J. McMahon<sup>1</sup>, R.A. McPherson<sup>28</sup>, F. Meijers<sup>8</sup>, S. Menke<sup>3</sup>, F.S. Merritt<sup>9</sup>, H. Mes<sup>7</sup>, J. Meyer<sup>27</sup>, A. Michelini<sup>2</sup>, S. Mihara<sup>24</sup>, G. Mikenberg<sup>26</sup>, D.J. Miller<sup>15</sup>, R. Mir<sup>26</sup>, W. Mohr<sup>10</sup>, A. Montanari<sup>2</sup>, T. Mori<sup>24</sup>, K. Nagai<sup>8</sup>, I. Nakamura<sup>24</sup>, H.A. Neal<sup>12</sup>, B. Nellen<sup>3</sup>, R. Nisius<sup>8</sup>, S.W. O’Neale<sup>1</sup>, F.G. Oakham<sup>7</sup>, F. Odorici<sup>2</sup>, H.O. Ogren<sup>12</sup>, M.J. Oreglia<sup>9</sup>, S. Orito<sup>24</sup>, J. Pálincás<sup>33,d</sup>, G. Pásztor<sup>32</sup>, J.R. Pater<sup>16</sup>, G.N. Patrick<sup>20</sup>, J. Patt<sup>10</sup>, R. Perez-Ochoa<sup>8</sup>, S. Petzold<sup>27</sup>, P. Pfeifenschneider<sup>14</sup>, J.E. Pilcher<sup>9</sup>, J. Pinfold<sup>30</sup>, D.E. Plane<sup>8</sup>, P. Poffenberger<sup>28</sup>, J. Polok<sup>8</sup>, M. Przybycień<sup>8</sup>, C. Rembser<sup>8</sup>, H. Rick<sup>8</sup>, S. Robertson<sup>28</sup>, S.A. Robins<sup>22</sup>, N. Rodning<sup>30</sup>, J.M. Roney<sup>28</sup>, K. Roscoe<sup>16</sup>, A.M. Rossi<sup>2</sup>, Y. Rozen<sup>22</sup>, K. Runge<sup>10</sup>, O. Runolfsson<sup>8</sup>, D.R. Rust<sup>12</sup>, K. Sachs<sup>10</sup>, T. Saeki<sup>24</sup>, O. Sahr<sup>34</sup>, W.M. Sang<sup>25</sup>, E.K.G. Sarkisyan<sup>23</sup>, C. Sbarra<sup>29</sup>, A.D. Schaile<sup>34</sup>, O. Schaile<sup>34</sup>, F. Scharf<sup>3</sup>, P. Scharff-Hansen<sup>8</sup>, J. Schieck<sup>11</sup>, B. Schmitt<sup>8</sup>, S. Schmitt<sup>11</sup>, A. Schönig<sup>8</sup>, M. Schröder<sup>8</sup>, M. Schumacher<sup>3</sup>, C. Schwick<sup>8</sup>, W.G. Scott<sup>20</sup>, T. Seiler<sup>10</sup>, R. Seuster<sup>14</sup>, T.G. Shears<sup>8</sup>, B.C. Shen<sup>4</sup>, C.H. Shepherd-Themistocleous<sup>8</sup>, P. Sherwood<sup>15</sup>, G.P. Siroli<sup>2</sup>, A. Sittler<sup>27</sup>, A. Skuja<sup>17</sup>, A.M. Smith<sup>8</sup>, G.A. Snow<sup>17</sup>, R. Sobie<sup>28</sup>, S. Söldner-Rembold<sup>10</sup>, M. Sproston<sup>20</sup>, A. Stahl<sup>3</sup>, K. Stephens<sup>16</sup>, J. Steuerer<sup>27</sup>, K. Stoll<sup>10</sup>,

D. Strom<sup>19</sup>, R. Ströhmer<sup>34</sup>, B. Surrow<sup>8</sup>, S.D. Talbot<sup>1</sup>, S. Tanaka<sup>24</sup>, P. Taras<sup>18</sup>, S. Tarem<sup>22</sup>,  
R. Teuscher<sup>8</sup>, M. Thiergen<sup>10</sup>, M.A. Thomson<sup>8</sup>, E. von Törne<sup>3</sup>, E. Torrence<sup>8</sup>, S. Towers<sup>6</sup>,  
I. Trigger<sup>18</sup>, Z. Trócsányi<sup>33</sup>, E. Tsur<sup>23</sup>, A.S. Turcot<sup>9</sup>, M.F. Turner-Watson<sup>8</sup>, R. Van Kooten<sup>12</sup>,  
P. Vannerem<sup>10</sup>, M. Verzocchi<sup>10</sup>, H. Voss<sup>3</sup>, F. Wäckerle<sup>10</sup>, A. Wagner<sup>27</sup>, C.P. Ward<sup>5</sup>, D.R. Ward<sup>5</sup>,  
P.M. Watkins<sup>1</sup>, A.T. Watson<sup>1</sup>, N.K. Watson<sup>1</sup>, P.S. Wells<sup>8</sup>, N. Wermes<sup>3</sup>, J.S. White<sup>6</sup>,  
G.W. Wilson<sup>16</sup>, J.A. Wilson<sup>1</sup>, T.R. Wyatt<sup>16</sup>, S. Yamashita<sup>24</sup>, G. Yekutieli<sup>26</sup>, V. Zacek<sup>18</sup>,  
D. Zer-Zion<sup>8</sup>

<sup>1</sup>School of Physics and Astronomy, University of Birmingham, Birmingham B15 2TT, UK

<sup>2</sup>Dipartimento di Fisica dell' Università di Bologna and INFN, I-40126 Bologna, Italy

<sup>3</sup>Physikalisches Institut, Universität Bonn, D-53115 Bonn, Germany

<sup>4</sup>Department of Physics, University of California, Riverside CA 92521, USA

<sup>5</sup>Cavendish Laboratory, Cambridge CB3 0HE, UK

<sup>6</sup>Ottawa-Carleton Institute for Physics, Department of Physics, Carleton University, Ottawa, Ontario K1S 5B6, Canada

<sup>7</sup>Centre for Research in Particle Physics, Carleton University, Ottawa, Ontario K1S 5B6, Canada

<sup>8</sup>CERN, European Organisation for Particle Physics, CH-1211 Geneva 23, Switzerland

<sup>9</sup>Enrico Fermi Institute and Department of Physics, University of Chicago, Chicago IL 60637, USA

<sup>10</sup>Fakultät für Physik, Albert Ludwigs Universität, D-79104 Freiburg, Germany

<sup>11</sup>Physikalisches Institut, Universität Heidelberg, D-69120 Heidelberg, Germany

<sup>12</sup>Indiana University, Department of Physics, Swain Hall West 117, Bloomington IN 47405, USA

<sup>13</sup>Queen Mary and Westfield College, University of London, London E1 4NS, UK

<sup>14</sup>Technische Hochschule Aachen, III Physikalisches Institut, Sommerfeldstrasse 26-28, D-52056 Aachen, Germany

<sup>15</sup>University College London, London WC1E 6BT, UK

<sup>16</sup>Department of Physics, Schuster Laboratory, The University, Manchester M13 9PL, UK

<sup>17</sup>Department of Physics, University of Maryland, College Park, MD 20742, USA

<sup>18</sup>Laboratoire de Physique Nucléaire, Université de Montréal, Montréal, Quebec H3C 3J7, Canada

<sup>19</sup>University of Oregon, Department of Physics, Eugene OR 97403, USA

<sup>20</sup>CLRC Rutherford Appleton Laboratory, Chilton, Didcot, Oxfordshire OX11 0QX, UK

<sup>22</sup>Department of Physics, Technion-Israel Institute of Technology, Haifa 32000, Israel

<sup>23</sup>Department of Physics and Astronomy, Tel Aviv University, Tel Aviv 69978, Israel

<sup>24</sup>International Centre for Elementary Particle Physics and Department of Physics, University of Tokyo, Tokyo 113, and Kobe University, Kobe 657, Japan

<sup>25</sup>Institute of Physical and Environmental Sciences, Brunel University, Uxbridge, Middlesex UB8 3PH, UK

<sup>26</sup>Particle Physics Department, Weizmann Institute of Science, Rehovot 76100, Israel

<sup>27</sup>Universität Hamburg/DESY, II Institut für Experimental Physik, Notkestrasse 85, D-22607 Hamburg, Germany

<sup>28</sup>University of Victoria, Department of Physics, P O Box 3055, Victoria BC V8W 3P6, Canada

<sup>29</sup>University of British Columbia, Department of Physics, Vancouver BC V6T 1Z1, Canada

<sup>30</sup>University of Alberta, Department of Physics, Edmonton AB T6G 2J1, Canada

<sup>31</sup>Duke University, Dept of Physics, Durham, NC 27708-0305, USA

<sup>32</sup>Research Institute for Particle and Nuclear Physics, H-1525 Budapest, P O Box 49, Hungary

<sup>33</sup>Institute of Nuclear Research, H-4001 Debrecen, P O Box 51, Hungary

<sup>34</sup>Ludwigs-Maximilians-Universität München, Sektion Physik, Am Coulombwall 1, D-85748 Garching, Germany

<sup>a</sup> and at TRIUMF, Vancouver, Canada V6T 2A3

<sup>b</sup> and Royal Society University Research Fellow

<sup>c</sup> and Institute of Nuclear Research, Debrecen, Hungary

<sup>d</sup> and Department of Experimental Physics, Lajos Kossuth University, Debrecen, Hungary

<sup>e</sup> on leave of absence from the University of Freiburg

## 1 Introduction

Single Z boson production in  $e^+e^-$  collisions [1],  $e^+e^- \rightarrow (e)eZ$ , will be the dominant source of Z bosons at linear  $e^+e^-$  colliders with centre-of-mass energies above 500 GeV [2]. At LEP2, however, the cross-section is nearly two orders of magnitude below the “radiative return” process  $e^+e^- \rightarrow \gamma Z$ . The elementary subprocess of single Z boson production is<sup>1</sup>  $e^- \gamma \rightarrow e^- Z$  where a quasi-real photon radiated from one of the beam electrons scatters off the other electron producing a Z as shown in Fig. 1. This process is ordinary Compton scattering with the outgoing real photon replaced by a Z. Its cross-section has first been calculated for ep collisions [3], where the incoming photon is radiated from the proton. Another variant of Compton scattering is  $e^- \gamma \rightarrow e^- \gamma^*$ , where this time the outgoing real photon is replaced by a virtual one. The observable final state  $(e)\text{eff}$  will in both cases be the scattered electron  $e$  and a fermion pair  $f\bar{f}$  from the  $Z/\gamma^*$  decay, while the other electron ( $e$ ) usually remains unobserved in the beam pipe.

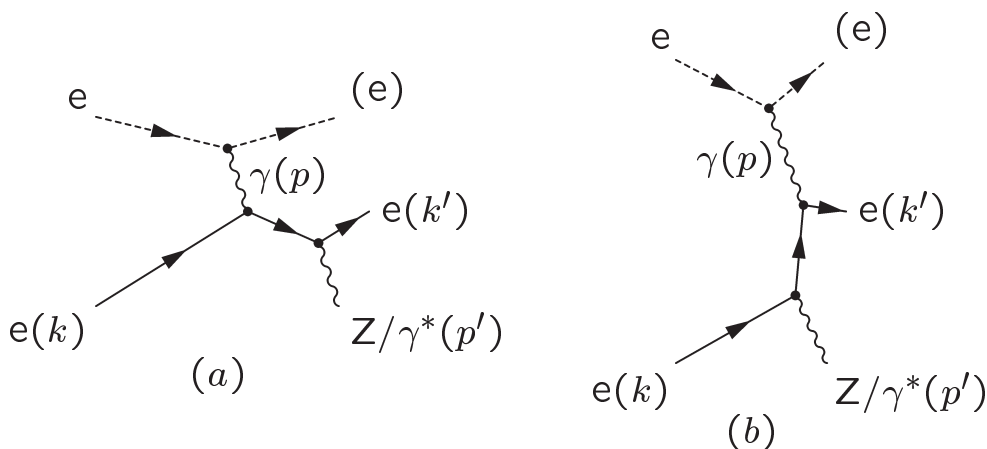


Figure 1: *Diagrams for the process  $e^+e^- \rightarrow (e)eZ/\gamma^*$ .*

<sup>1</sup>Charge conjugation is implied throughout the paper except when otherwise stated.

The final state  $(e)\text{eff}\bar{f}$  may contribute an important background to many searches for new physics, for example final states involving large missing masses ( $\text{ff} = \nu\bar{\nu}$ ), leptoquark production in deep inelastic electron-photon scattering ( $\text{ff} = q\bar{q}$ ), new particles decaying to Z bosons, and excited electrons in the decay channel  $\text{eff}$ . Excited electrons can for example directly contribute in the  $\hat{s}$  and  $\hat{u}$  channel diagrams of the signal in Fig. 1.

For Z boson production in Compton scattering  $e(k)\gamma(p) \rightarrow e(k')Z(p')$  of real photons ( $p^2 = 0$ ), the cross-section dependence on the Mandelstam variables  $\hat{s} = (k'+p')^2$ ,  $\hat{t} = (k'-k)^2$ ,  $\hat{u} = (p'-k)^2$  is [3]

$$\frac{d\sigma}{d\hat{t}} \propto \frac{1}{\hat{s}^2} \left( \frac{\hat{u}}{\hat{s}} + \frac{2M_Z^2\hat{t}}{\hat{u}\hat{s}} + \frac{\hat{s}}{\hat{u}} \right). \quad (1)$$

For  $M_Z = 0$  the well-known terms for ordinary Compton scattering remain. The typical transverse momentum scale of the scattered  $Z/\gamma^*$  bosons is small, leading to a singularity at  $\hat{u} = 0$  of the virtual electron propagator in Fig. 1b. For incoming quasi-real photons ( $p^2 \approx 0$ ) in ep or  $e^+e^-$  collisions, the dominant regulating effect for this divergence is not the electron mass, but small, non-zero, incoming photon masses squared  $p^2$ , which introduce via the replacement [3]

$$\hat{u} \rightarrow \hat{u} + p^2 \frac{M_Z^2}{\hat{s}} \quad (2)$$

a lower cutoff in the denominator of Eq. (1). A simple equivalent photon approximation (EPA), as used in Ref. [4], where the integration over the range of small photon virtualities leads to an effective on-shell incoming photon flux, overestimates the cross-section by about a factor of two [2]. In order to properly describe the process, the  $p^2$  spectrum of the incoming photons has to be retained fully, or a modified EPA [2] has to be introduced. In any case the results will be sensitive to the modelling of the  $p^2$  spectrum. In this paper the theoretical expectations are represented by Monte Carlo event generators which use different approaches for obtaining the  $p^2$  spectrum of the incoming photons. These are compared with experimental data for the first time.

We have analysed the process  $e^+e^- \rightarrow (e)eZ/\gamma^*$  using data collected with the OPAL detector at an  $e^+e^-$  centre-of-mass energy of about 183 GeV, corresponding to a total integrated luminosity of approximately  $55 \text{ pb}^{-1}$ . The Z or the  $\gamma^*$  is observed via its decay to hadrons.

## 2 The OPAL detector

A detailed description of the OPAL detector can be found elsewhere [5]. Subdetectors which are particularly relevant for the present analysis are described here briefly. The central detector consists of a system of tracking chambers providing charged particle tracking over 96% of the full solid angle inside a 0.435 T uniform magnetic field parallel to the beam axis<sup>2</sup>. Starting with the innermost components, it consists of a high precision silicon microvertex detector, a precision vertex drift chamber, a large volume jet chamber with 159 layers of axial anode wires and a set of  $z$  chambers measuring the track coordinates along the beam direction. With the jet chamber,

<sup>2</sup>The OPAL coordinate system is a right-handed system which is defined such that the  $z$ -axis is in the direction of the electron beam and the  $x$ -axis is horizontal and points towards the centre of the LEP ring;  $\theta$  is the polar angle with respect to  $z$  and  $\phi$  is the azimuthal angle about the  $z$  axis.

the momenta of tracks can be measured with an accuracy of  $\sigma_p/p^2 = 2 \times 10^{-3} \text{ GeV}^{-1}$ . The jet chamber also provides energy loss measurements which are used for particle identification.

A lead-glass electromagnetic calorimeter (ECAL) located outside the magnet coil covers the full azimuthal range with excellent hermeticity in the polar angle range of  $|\cos\theta| < 0.82$  for the barrel region and  $0.81 < |\cos\theta| < 0.984$  for the endcap region. The forward detectors and silicon tungsten calorimeters [6] located at both sides of the interaction point measure the integrated luminosity and complete the geometrical acceptance down to 33 mrad in polar angle. The magnet return yoke is instrumented with streamer tubes for hadron calorimetry and is surrounded by several layers of muon chambers.

### 3 Event simulation

The  $e^+e^- \rightarrow (e)eZ/\gamma^*$  signal events are generated using the grc4f Monte Carlo program [7]. Hadronization is performed by JETSET [8]. A sample of approximately 170 times the integrated luminosity of the data was used. In grc4f, an automatic computation system for Feynman diagrams, GRACE [9] is invoked, yielding the differential cross-sections of tree-level diagrams by performing a calculation of the matrix elements and a Monte Carlo integration over the phase space. Initial state radiation corrections are also implemented. The delicate  $p^2$  distribution of the incoming photons for the  $e\gamma$  Compton scattering is thus obtained by a numerical integration of the matrix element.

As a second Monte Carlo event generator for the process  $e^+e^- \rightarrow (e)eZ/\gamma^*$  we used the PYTHIA [10] program. To include the full phase space for this low- $p_t$  process, we lowered the  $\hat{p}_t$  cutoff in the  $e\gamma$  rest frame from the default of 1 GeV to 10 MeV in the generation of the events, as suggested in the PYTHIA manual. Without this change PYTHIA would underestimate largely the cross-section. In PYTHIA, the signal process is simulated according to Eqs. (1) and (2). An equivalent flow of incoming photons is modelled with a  $p^2$  distribution obtained from a first order QED expression [10]. This approximation implemented in PYTHIA is used as a cross-check, with a sample size of about 1/10 of that generated with grc4f.

Backgrounds from other four-fermion final states have been studied using several samples also generated with grc4f and JETSET. Background contributions from two-photon processes,  $e^+e^- \rightarrow e^+e^- + \text{hadrons}$ , were evaluated using PHOJET [11] for events with low  $Q^2$  and HERWIG [12] for high- $Q^2$  processes. Double counting of the  $eeq\bar{q}$  final state between signal, two-photon and other four-fermion samples is avoided by separating the contributions from different classes of diagrams, or by performing kinematic cuts. Two-photon production of  $\tau^+\tau^-$  was modelled with the VERMASEREN [13] generator. Other background processes involving two fermions in the final state were simulated using PYTHIA for the channel  $e^+e^- \rightarrow q\bar{q}$  and KORALZ [14] for the channel  $e^+e^- \rightarrow \tau^+\tau^-$ . Background contributions from other processes have been checked and found to be negligible.

All Monte Carlo events were passed through the full simulation of the OPAL detector [15] and then subjected to the same reconstruction and analysis procedures as the real data.

## 4 Signal definition

In most of the  $e^+e^- \rightarrow (e)eZ/\gamma^*$  events the first incoming electron, which radiates the photon taking part in the Compton process, remains undetected in the beam pipe due to the low momentum transfer  $p^2$ . In contrast, the second electron is often emitted at large angles. Therefore the predominant signature of the process is a single scattered electron isolated from a hadronic system containing one or two hadron jets from the  $Z/\gamma^*$  decay. The differential distribution is peaked at low  $p'^2$  (low mass  $q\bar{q}$  systems) and at low  $|\hat{u}|$  where the outgoing  $Z/\gamma^*$  is emitted almost in the direction of the second incoming electron. Since for low  $p'^2$  and low  $|\hat{u}|$  a huge part of the cross-section remains unobserved in the beam pipe, it is not practical to measure the signal process  $e^+e^- \rightarrow (e)eZ/\gamma^*$  in the whole phase space corresponding to the diagrams in Fig. 1. Furthermore, considerable uncertainties due to hadronic resonances for low mass  $\gamma^*$  provide a supplementary reason for limiting the phase space. The  $e^+e^- \rightarrow (e)eZ/\gamma^*$  signal process is therefore defined by the diagrams in Fig. 1 and by applying the following additional kinematic cuts on the  $eeq\bar{q}$  final state.

- One of the primary electrons is required to remain in the beam pipe:  $|\cos\theta_{e_1}| > 0.9995$ . This angular cut is chosen close to the edge of the silicon tungsten calorimeter.
- The second beam electron has to form a large angle with respect to the beam:  $|\cos\theta_{e_2}| < 0.985$ , corresponding to the edge of the electromagnetic endcap calorimeter.
- In order to detect the hadronic final state from the  $Z/\gamma^*$  decay, we demand at least one primary quark with  $|\cos\theta_q| < 0.985$ .
- We require the invariant mass of the primary quark pair to be greater than 5 GeV.

The cross-section times branching ratio predicted for  $e^+e^- \rightarrow (e)eZ/\gamma^*$  events with an  $eeq\bar{q}$  final state satisfying the signal definition has been evaluated using the `grc4f` and `PYTHIA` programs at an  $e^+e^-$  centre-of-mass energy of 183 GeV. We obtain values of  $(4.80 \pm 0.02)$  pb for `grc4f` and  $(4.76 \pm 0.04)$  pb for `PYTHIA`.

In addition to the  $e\gamma$  Compton scattering in the process  $e^+e^- \rightarrow (e)eZ/\gamma^*$ , there are two other classes of processes which lead to an  $eeq\bar{q}$  final state, namely  $e^+e^-$  annihilation, dominated by  $Z/\gamma^* - Z/\gamma^*$  intermediate states, and two-photon interactions. Of the former process, only a negligible cross-section of 0.002 pb fulfils the kinematic cuts of our signal definition, since the topology with exactly one electron very close to the beam direction and the other electron visible at large angles is not preferred. Among the two-photon interactions, on the other hand, exactly this “single-tagged” topology is typical for deep inelastic  $e\gamma$  scattering with large momentum transfer squared<sup>3</sup>,  $q^2 \equiv -Q^2$ . According to `PHOJET` and `HERWIG`, two-photon events which satisfy the above kinematic cuts are produced with a cross-section of approximately 5.6 pb.

Using `grc4f` we checked that possible interferences between the different classes of Feynman diagrams contributing to the  $eeq\bar{q}$  final state,  $e\gamma$  Compton scattering,  $e^+e^-$  annihilation, and two-photon interaction, are negligible. It is therefore justified to treat each process separately

---

<sup>3</sup>Note, that  $q^2$  in two-photon processes is by definition identical to  $\hat{t}$  in our signal process.

and to add the predictions of the respective Monte Carlo generators. Only  $e^+e^- \rightarrow (e)eZ/\gamma^*$  events which fulfil the signal definition are treated as “signal”. All other processes leading to an  $eeq\bar{q}$  final state are treated as “background” even if the kinematic signal definition is fulfilled. Likewise,  $e^+e^- \rightarrow (e)eZ/\gamma^*$  events that do not fulfil the signal definition are treated as “background”.

## 5 Event preselection

We perform a preselection of events with a hadronic final state and an isolated electron candidate. Only tracks and clusters which satisfy standard quality criteria are considered in the analysis. The following preselection cuts are applied.

- We reject low multiplicity events by requiring the sum  $N_{\text{mult}}$  of the number of tracks and electromagnetic clusters not associated with any track to be greater than 8.
- We search for electron candidates among all tracks using the following criteria. We require the probability of the measured ionization energy loss  $dE/dx$  of the track being consistent with an electron hypothesis to be greater than 5%. Furthermore we require  $E_e/p_e > 0.6$  where  $E_e$  is the total energy in the electromagnetic calorimeter associated with the track and  $p_e$  is the track momentum. For all electron candidate tracks we define a cone energy  $E_{\text{cone}}$  as the sum of all track momenta and electromagnetic cluster energies in a cone with a half angle of 0.2 rad around the track, excluding the momentum and the cluster energy associated to the electron candidate track. If more than one candidate is found in an event, the one which has the smallest  $E_{\text{cone}}$  is chosen as the signal electron. To suppress events with fake electron candidates, we require the angle between the signal electron and the closest track to be greater than 0.25 rad and  $E_e$  to be larger than 2 GeV.
- In order to be consistent with the signal definition, we require the invariant mass of the  $q\bar{q}$  system  $m_{q\bar{q}}$  to be larger than 5 GeV. This mass is calculated from the momentum of all tracks and the energy deposited in the electromagnetic and hadronic calorimeters, the forward detectors and silicon tungsten calorimeters, excluding those associated with the signal electron, using an algorithm [16] which corrects for double counting of energy between tracks and calorimeter clusters.

In Fig. 2 we compare the measured distributions of  $m_{q\bar{q}}$  and  $E_e$  after preselection with the corresponding Monte Carlo expectations. The gross features of the data are in satisfactory agreement with the prediction at this early stage of the analysis. Discrepancies, especially at low values of  $m_{q\bar{q}}$  and  $E_e$ , can be attributed to systematic uncertainties in the two-photon process  $e^+e^- \rightarrow e^+e^- + \text{hadrons}$  which is difficult to model in this kinematic region. The apparent excess of Monte Carlo events in the range  $105 \text{ GeV} < m_{q\bar{q}} < 160 \text{ GeV}$  has no influence on the analysis, since it is populated nearly exclusively by background events, which will be rejected later on. A total of  $1558 \pm 25$  events is expected, where the main contributions are from two-photon interactions,  $e^+e^- \rightarrow W^+W^-$  and multihadronic events. In the data 1882 events are found after the preselection (see Table 1). As seen from Fig. 2, the data excess is located in kinematic regions where the two-photon background dominates.

The expected signal contribution is  $38.0 \pm 0.5$   $e^+e^- \rightarrow (e)eZ/\gamma^*$  events, corresponding to an average signal efficiency of  $(14.5 \pm 0.2)\%$  obtained with the `grc4f` Monte Carlo program. The corresponding value obtained from PYTHIA is  $(16.7 \pm 0.6)\%$ . A large part of the preselection inefficiency for all  $Z/\gamma^*$  masses is due to the typical small transverse momenta of the electron and the  $Z/\gamma^*$  in the final state. Signal electrons which form large angles with respect to the beam therefore often have momenta below 2 GeV. In addition, for low  $\gamma^*$  masses, the  $\gamma^*$  decay products tend to be in a rather narrow cone preferring forward directions, where particles may escape undetected along the beam pipe. As a result many of these events fail the multiplicity cut. This reflects in a significantly lower preselection efficiency for smaller hadronic masses. Considering only signal events with  $m_{q\bar{q}} < 60$  GeV, `grc4f` predicts the preselection efficiency to be  $(9.5 \pm 0.2)\%$ , while for  $m_{q\bar{q}} > 60$  GeV the efficiency is  $(50.3 \pm 0.7)\%$ . The PYTHIA prediction is consistent with these numbers.

Cut	Number of expected events from MC						OPAL data
	(e)eZ/ $\gamma^*$	$\gamma\gamma$	$q\bar{q}$	4f	other	Sum	
Preselection	$38.0 \pm 0.5$	$1251.9 \pm 23.9$	$113.8 \pm 3.6$	$143.1 \pm 0.9$	$11.6 \pm 0.6$	$1558.4 \pm 24.7$	1882
$-\mathbf{Q}_e \cdot \cos \theta_{q\bar{q}} > 0.75$	$33.0 \pm 0.4$	$575.0 \pm 16.5$	$42.6 \pm 2.2$	$11.6 \pm 0.3$	$3.5 \pm 0.4$	$665.7 \pm 16.7$	766
$-\mathbf{Q}_e \cdot \cos \theta_e < 0.75$	$26.5 \pm 0.4$	$209.5 \pm 10.1$	$30.8 \pm 1.9$	$9.3 \pm 0.2$	$2.0 \pm 0.3$	$278.1 \pm 10.3$	294
$ \cos \theta_{\text{miss}}  > 0.95$	$24.3 \pm 0.4$	$128.9 \pm 7.8$	$20.2 \pm 1.5$	$2.9 \pm 0.1$	$1.1 \pm 0.2$	$177.5 \pm 7.9$	193
$p_{\text{miss}} > 30$ GeV	$21.6 \pm 0.3$	$21.0 \pm 2.0$	$15.9 \pm 1.4$	$2.0 \pm 0.1$	$0.7 \pm 0.1$	$61.2 \pm 2.5$	74
electron isolation	$17.5 \pm 0.3$	$8.2 \pm 1.2$	$1.9 \pm 0.5$	$1.4 \pm 0.1$	$0.6 \pm 0.1$	$29.6 \pm 1.3$	36
$E_{\text{fwd}} < 35$ GeV	$16.7 \pm 0.3$	$3.1 \pm 0.8$	$1.8 \pm 0.5$	$1.4 \pm 0.1$	$0.3 \pm 0.1$	$23.2 \pm 0.9$	27

Table 1: Numbers of expected and observed events for a luminosity of  $55 \text{ pb}^{-1}$  after application of each cut. Only the most important sources of background are shown separately. The number of expected signal events is obtained using the `grc4f` generator. The numbers of background events are evaluated using the Monte Carlo samples (MC) described in the text. The errors are statistical only.

## 6 Selection of $e^+e^- \rightarrow (e)eZ/\gamma^*$ events

In order to reduce the remaining background six further cuts have been applied which can be divided into three groups. The first group consists the following angular cuts.

- In the  $e^+e^- \rightarrow (e)eZ/\gamma^*$  signal process, the  $Z/\gamma^*$  is usually scattered very close to the beam direction of the detected signal electron, given by  $-\mathbf{Q}_e \cdot \cos \theta = 1$ , where  $\mathbf{Q}_e$  is the charge (in units of  $e$ ) of the signal electron. We therefore require  $-\mathbf{Q}_e \cdot \cos \theta_{q\bar{q}} > 0.75$ , where  $\cos \theta_{q\bar{q}}$  is the cosine of the polar angle of the  $q\bar{q}$  system (see Fig. 3a).
- To suppress the otherwise irreducible background of single-tagged two-photon events, which fulfil the kinematic signal definition, we take advantage of the fact that the distribution of the polar angle  $\cos \theta_e$  of the tagged electrons peaks around their beam direction. We thus only retain events where  $-\mathbf{Q}_e \cdot \cos \theta_e$  is less than 0.75. This cut is shown in Fig. 3b. Note that two-photon events with fake electrons, distributed symmetrically in  $-\mathbf{Q}_e \cdot \cos \theta_e$ , largely dominate this spectrum. Correctly identified tagged electrons of high  $Q^2$  two-photon events are visible as an asymmetry in the region near +1.

Signal events are further characterised by an undetected electron along the beam direction, so that cuts on the direction and amount of the missing momentum in the event can be applied.

- We require the absolute value of the cosine of the polar angle of the missing momentum  $|\cos\theta_{\text{miss}}|$  to be larger than 0.95 (see Fig. 3c). The largest relative suppression of this cut occurs for  $e^+e^- \rightarrow W^+W^-$  events, where one W boson decays to hadrons and the other to an electron and a neutrino, since the neutrino is not preferentially emitted close to the beam direction.
- The distribution of the missing momentum after the cut on  $|\cos\theta_{\text{miss}}|$  is shown in Fig. 3d. Requiring a missing momentum of at least 30 GeV largely suppresses remaining background with fake or conversion electrons from untagged two-photon events where both beam electrons stay under small angles with respect to the beam axis and tend to balance the momentum.

The third group of cuts is applied to suppress events with fake electron candidates.

- The minimum angle between the electron and the nearest charged track was required to be 0.65 rad. This cut removes most of the remaining multihadronic background as shown in Fig. 3e.
- The sample still includes a small amount of two-photon background tagged by an electron in the forward calorimeters where the signal electron is fake or due to a double-tagged event topology. It is suppressed significantly by requiring the total energy deposit in the forward detectors and silicon tungsten calorimeters,  $E_{\text{fwd}}$ , not to exceed 35 GeV (see Fig. 3f).

The cuts, together with the expected and observed numbers of events, are shown in Table 1. Already after the second cut there remains no significant excess in the data compared with the expectation. The six selection cuts improve the signal to background ratio by about a factor of 100 compared with the preselection, while retaining about half of the signal events.

The efficiencies after all cuts are given in Table 2. Considering only signal events with  $m_{q\bar{q}} < 60$  GeV, dominated by  $(e)e\gamma^*$ , grc4f predicts an overall selection efficiency of  $(4.1\pm 0.1)\%$ . For  $m_{q\bar{q}} > 60$  GeV, dominated by  $(e)eZ$ , the overall efficiency is  $(22.3\pm 0.6)\%$ . The corresponding numbers from PYTHIA,  $(4.3\pm 0.3)\%$  and  $(22.3\pm 1.7)\%$ , are consistent with grc4f within their statistical errors. From the two lowest lines in Table 2, however, it is evident that PYTHIA predicts a slightly different mix of high mass “eeZ”-type and low mass “ee $\gamma^*$ ”-type events than grc4f. This causes about a 15% relative difference between the two Monte Carlo generators for efficiencies averaged over the total  $m_{q\bar{q}}$  range and explains the differences in the total preselection efficiencies given at the end of Section 5. Since the predicted efficiency of each single cut is consistent between the two simulations, this difference remains essentially unchanged after the final selection cuts.

For calculating cross-sections we avoid assumptions on the mix of “eeZ”-type, and “ee $\gamma^*$ ”-type events. We instead calculate the cross-sections separately, for masses above and below 60 GeV, the point where the differential  $m_{q\bar{q}}$  distribution has its minimum, using the efficiencies

obtained from grc4f. After correcting for feed-through from the low to the high mass region, and vice versa, we obtain the results listed in Table 2. The measured cross-sections agree with the predictions of the two Monte Carlo generators.

	$5 \text{ GeV} < m_{q\bar{q}} < 60 \text{ GeV}$ “ $ee\gamma^*$ ”	$m_{q\bar{q}} \geq 60 \text{ GeV}$ “ $eeZ$ ”
efficiency (%)	$4.1 \pm 0.1$	$22.3 \pm 0.6$
signal expected	$9.5 \pm 0.2$	$7.2 \pm 0.2$
background	$4.4 \pm 0.8$	$2.1 \pm 0.4$
feed-through from neighbouring mass region	0.2	0.1
OPAL data	14	13
cross-section (measured) (pb)	$4.1 \pm 1.6$	$0.9 \pm 0.3$
cross-section (grc4f) (pb)	$4.21 \pm 0.02$	$0.59 \pm 0.01$
cross-section (PYTHIA) (pb)	$4.04 \pm 0.03$	$0.72 \pm 0.02$

Table 2: Comparison of the OPAL data with the cross-sections predicted by the grc4f and the PYTHIA Monte Carlo generators for  $5 \text{ GeV} < m_{q\bar{q}} < 60 \text{ GeV}$  (“ $ee\gamma^*$ ” region) and for  $m_{q\bar{q}} \geq 60 \text{ GeV}$  (“ $eeZ$ ” region). The efficiencies have been obtained with grc4f. Only statistical errors are given. The errors on the feed-through are negligible.

In Fig. 4 we have plotted after all cuts the same distributions as in Fig. 2. The respective contributions of the  $\gamma^*$  and of the  $Z$  to the measured process are clearly visible in the  $m_{q\bar{q}}$  distribution. The  $E_e$  distribution shows the preference for small electron momenta due to the low transverse momenta involved in the  $e\gamma$  scattering.

## 7 Systematic studies

Several sources of systematic errors have been considered. Uncertainties in the description of the signal process may cause a systematic error on the efficiencies. These come mainly from imperfect modelling of the detector and have been analysed by comparing the Monte Carlo simulation to real data for the process  $e^+e^- \rightarrow W^+W^-$  where one  $W$  decays hadronically and the other one to an electron and a neutrino. This process has the same observable final state as  $e^+e^- \rightarrow (e)eZ/\gamma^*$  and can therefore be used to check for any discrepancies in the description of the cut variables which would lead to an error in the selection efficiency. After selecting the  $e^+e^- \rightarrow W^+W^- \rightarrow q\bar{q}e^-\bar{\nu}_e$  events using the procedure described in Ref. [17], each cut was applied separately to this sample. The difference in selection efficiency between data and the Monte Carlo simulation was taken as the systematic error after subtracting quadratically the statistical error of the  $WW$  sample. In those cases where the statistical error was larger than the efficiency differences, we have conservatively taken the statistical error as systematic uncertainty. The results of the check are shown in Table 3. In our error estimate we have considered the fact that some distributions of the process  $e^+e^- \rightarrow W^+W^- \rightarrow q\bar{q}e^-\bar{\nu}_e$  are significantly different from those of the signal (e.g.  $-\mathcal{Q}_e \cdot \cos \theta_{q\bar{q}}$  or  $|\cos \theta_{\text{miss}}|$ ). These systematic uncertainties have been used for both the “ $ee\gamma^*$ ”-like and the “ $eeZ$ ”-like hadronic mass region, since the efficiencies of each selection cut are similar in the two regions. As mentioned above,

the relatively smaller overall efficiency for “ $ee\gamma^*$ ”-like events is due to the multiplicity cut in the preselection. To assess the systematic uncertainty of this cut, we have calculated the change in efficiency when the simulated  $N_{\text{mult}}$  distribution is shifted by  $\pm 1$ . Half of the resulting change is quoted as uncertainty for this cut in the first row of Table 3. The total relative systematic uncertainty on the signal efficiencies due to event simulation is then found to be 0.086 for high mass and 0.107 for low mass hadronic systems, respectively.

	$5 \text{ GeV} < m_{q\bar{q}} < 60 \text{ GeV}$ “ $ee\gamma^*$ ”	$m_{q\bar{q}} \geq 60 \text{ GeV}$ “ $eeZ$ ”
$N_{\text{mult}} > 8$	0.063	0.000
$-Q_e \cdot \cos \theta_{q\bar{q}} > 0.75$	0.018	0.018
$-Q_e \cdot \cos \theta_e < 0.75$	0.037	0.037
$ \cos \theta_{\text{miss}}  > 0.95$	0.047	0.047
$p_{\text{miss}} > 30 \text{ GeV}$	0.036	0.036
electron isolation	0.046	0.046
$E_{\text{fwd}} < 35 \text{ GeV}$	0.009	0.009
event simulation	0.107	0.086
generator distributions	0.063	0.063
background	0.070	0.018
Total	0.142	0.108

Table 3: *Relative systematic uncertainties of the cross-section measurements. The entry “event simulation” is the quadratic sum of the signal efficiency uncertainties for the single cuts listed in the rows above it.*

A smaller contribution is the uncertainty of the efficiency due to systematic errors in the Monte Carlo generator distributions. This has been estimated from the relative difference between the measured “ $ee\gamma^*$ ” and “ $eeZ$ ” cross-sections obtained using the efficiencies from grc4f and those from PYTHIA. The relative cross-section differences are very similar in both hadronic mass regions, and statistically compatible with zero. Adding the cross-sections of both regions, a relative difference of  $0.033 \pm 0.063$  between grc4f and PYTHIA is found. In Table 3 we conservatively take the statistical error on this difference as systematic uncertainty for both the “ $ee\gamma^*$ ” and the “ $eeZ$ ” region.

Uncertainties in the description of the background processes cause systematic errors on the background subtraction. The contributions to these errors coming from  $e^+e^- \rightarrow q\bar{q}$ , two-photon processes and other four-fermion backgrounds have been tested separately for each background. By inverting or removing one or two selection cuts while the others were left unchanged, we produced samples where the analysed background process is significantly dominant. We obtained the systematic uncertainty for the various background processes by taking the relative difference of the total event numbers in data and Monte Carlo after the statistical error on the data has been subtracted quadratically. The relative systematic uncertainties we obtain are 0.17 for the  $e^+e^- \rightarrow q\bar{q}$  background, 0.14 for the four-fermion backgrounds and 0.24 for the two-photon process  $e^+e^- \rightarrow e^+e^- + \text{hadrons}$ . The numbers of background events after all cuts are  $1.8 \pm 0.5 \pm 0.3$ ,  $1.4 \pm 0.1 \pm 0.2$  and  $3.1 \pm 0.8 \pm 0.7$  for  $e^+e^- \rightarrow q\bar{q}$ ,  $e^+e^- \rightarrow 4f$  and  $e^+e^- \rightarrow e^+e^- + \text{hadrons}$ , respectively. Since other background sources are much smaller, their systematic uncertainties have been neglected. The total error on the background events corresponds to a relative systematic uncertainty for the obtained cross-sections of 0.070 for “ $ee\gamma^*$ ” and 0.018 for “ $eeZ$ ” (see Table 3).

## 8 Results and conclusion

Using a data set with an integrated luminosity of  $(54.7 \pm 0.1 \pm 0.2)$   $\text{pb}^{-1}$  collected with the OPAL detector at  $\sqrt{s} = 183$  GeV, 27 candidate events for the process  $e^+e^- \rightarrow (e)eZ/\gamma^*$  have been selected, with an expected background of  $6.5 \pm 0.9 \pm 0.8$  events, where the first errors are statistical and the second are systematic. The expected number of signal events is  $16.7 \pm 0.3 \pm 1.9$ .

From the observed number of events, the cross-section for this process has been calculated separately for a high mass, “eeZ”-like, and a low mass, “ee $\gamma^*$ ”-like region, with a cut at a hadronic mass of 60 GeV. Within the phase space of our kinematic signal definition described in Section 4, we measure a cross-section of  $(4.1 \pm 1.6 \pm 0.6)$  pb for “ee $\gamma^*$ ”-like events, and a cross-section of  $(0.9 \pm 0.3 \pm 0.1)$  pb for “eeZ”-like events, including the systematic errors obtained in Section 7.

To investigate in more detail the kinematic properties of the Compton scattering process, we show in Fig. 5 the differential distributions of the Mandelstam variables from Equation 1, and of the cosine of the scattering angle  $\theta^*$  of the  $Z/\gamma^*$  in the  $e\gamma$  rest system with respect to the incoming  $\gamma$  direction. All quantities have been obtained from the measured momenta and energies of the electron and the hadronic system, and are compared with the grc4f signal prediction. The structure observed in the  $\sqrt{\hat{s}}$  distribution is consistent with expectation for the  $\gamma^*$  (low  $\sqrt{\hat{s}}$ ) and Z (high  $\sqrt{\hat{s}}$ ) contributions. An excited electron, contributing in the  $\hat{s}$ -channel of the signal diagram, would show up as a peak at the  $e^*$  mass. For illustration, we have added in Fig. 5a as a dashed histogram the expected contribution of events with an excited electron of mass  $m_e^* = 120$  GeV, normalized to a product of cross-section times branching ratio of 5 pb. It has been obtained by applying our analysis to fully simulated events of the process  $e^+e^- \rightarrow ee^* \rightarrow eeZ$  from the Monte Carlo generator EXOTIC [18].

In the  $\hat{t}$  and  $\hat{u}$  distributions, peaks near zero are predicted, with a long tail to large negative values in the case of  $\hat{t}$ . The measured  $\hat{t}$  distribution agrees well with this prediction and also shows the drop near zero, due to angular acceptance cuts. The observed  $\hat{u}$  distribution seems somewhat broader than predicted, though it is still consistent within errors. The entries at positive values are due to detector resolution. The distribution of  $\cos\theta^*$  peaks at  $-1$ , corresponding to small  $\hat{u}$  which is typical for Compton processes.

In summary, we have reported the first observation of  $Z/\gamma^*$  production in Compton scattering of quasi-real photons which is a subprocess of the reaction  $e^+e^- \rightarrow (e)eZ/\gamma^*$ . The predictions of the grc4f and PYTHIA Monte Carlo programs, as listed in Table 2, are both in good agreement with our results. The data statistics are not yet sufficient to be sensitive to the difference between the predictions of the Monte Carlo generators.

## Acknowledgements

We thank T. Sjöstrand for the useful discussions.

We particularly wish to thank the SL Division for the efficient operation of the LEP accelerator at all energies and for their continuing close cooperation with our experimental group. We

thank our colleagues from CEA, DAPNIA/SPP, CE-Saclay for their efforts over the years on the time-of-flight and trigger systems which we continue to use. In addition to the support staff at our own institutions we are pleased to acknowledge the  
Department of Energy, USA,  
National Science Foundation, USA,  
Particle Physics and Astronomy Research Council, UK,  
Natural Sciences and Engineering Research Council, Canada,  
Israel Science Foundation, administered by the Israel Academy of Science and Humanities,  
Minerva Gesellschaft,  
Benozio Center for High Energy Physics,  
Japanese Ministry of Education, Science and Culture (the Monbusho) and a grant under the Monbusho International Science Research Program,  
German Israeli Bi-national Science Foundation (GIF),  
Bundesministerium für Bildung, Wissenschaft, Forschung und Technologie, Germany,  
National Research Council of Canada,  
Research Corporation, USA,  
Hungarian Foundation for Scientific Research, OTKA T-016660, T023793 and OTKA F-023259.

## References

- [1] E. Gabrielli, “Single Weak Boson Production at CLIC”, CERN Yellow Report 87-07, Vol II (1987) 1.
- [2] K. Hagiwara et al., Nucl. Phys. B365 (1991) 544.
- [3] G. Altarelli, G. Martinelli, B. Mele, and R. Rückl, Nucl. Phys. B 262 (1985) 204; E. Gabrielli, Mod. Phys. Lett. A1 (1986) 465.
- [4] P. Salati and J.C. Wallet, Z. Phys. C16 (1982) 155.
- [5] OPAL Collaboration, K. Ahmet et al., Nucl. Instr. Meth. A305 (1991) 275.
- [6] B.E. Anderson et al., IEEE Trans. Nucl. Sci. 41 (1994) 845.
- [7] J. Fujimoto et al., Comp. Phys. Comm. 100 1997 128.
- [8] JETSET version 7.408; T. Sjöstrand, Comp. Phys. Comm. 82 (1994) 74.
- [9] T. Ishikawa et al., “The GRACE manual”, KEK Report 92-19, 1993.
- [10] PYTHIA version 5.722; T. Sjöstrand, Comp. Phys. Comm. 82 (1994) 74.  
A bug in this PYTHIA version concerning the decay branching ratios of the final state  $\gamma^*$  in the process  $e^+e^- \rightarrow e^+e^-\gamma^*$  was fixed with the help of the author.
- [11] R. Engel and J. Ranft, Phys. Rev. D54 (1996) 4244;  
R. Engel, Z. Phys. C66 (1995) 203.
- [12] G. Marchesini et al., Comp. Phys. Comm. 67 (1992) 465.

- [13] R. Bhattacharya, J. Smith and G. Grammer, Phys. Rev. D15 (1977) 3267;  
J. Smith, J.A.M. Vermaseren and G. Grammer, Phys. Rev. D15 (1977) 3280;  
J.A.M. Vermaseren, Nucl. Phys. B229 (1983) 347.
- [14] S. Jadach, B.F.L. Ward and Z. Wąs, Comp. Phys. Comm. 79 (1994) 503.
- [15] J. Allison et al., Nucl. Instr. Meth. A317 (1992) 47.
- [16] OPAL Collaboration, M. Z. Akrawy et al., Phys. Lett. B253 (1991) 511.
- [17] OPAL Collaboration, K. Ackerstaff et al., Eur. Phys. J. C1 (1998) 395.
- [18] OPAL Collaboration, K. Ackerstaff et al., Eur. Phys. J. C1 (1998) 45.

# OPAL

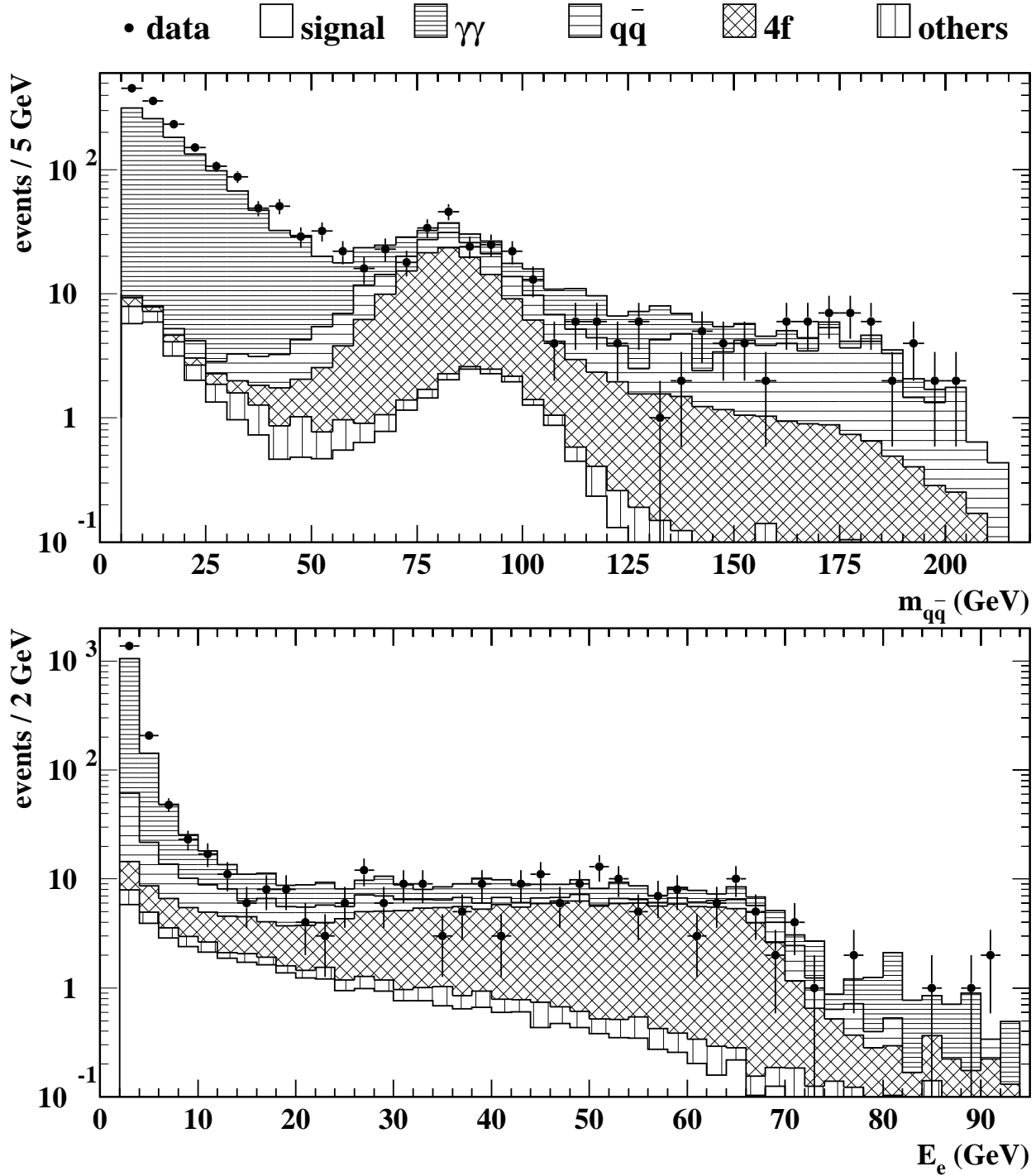


Figure 2: Distributions of  $m_{q\bar{q}}$  and  $E_e$  after the preselection. The histograms show the contributions from the various Monte Carlo simulations and the points are the data. The sharp lower edges of the spectra are due to preselection cuts. Only statistical errors are shown.

# OPAL

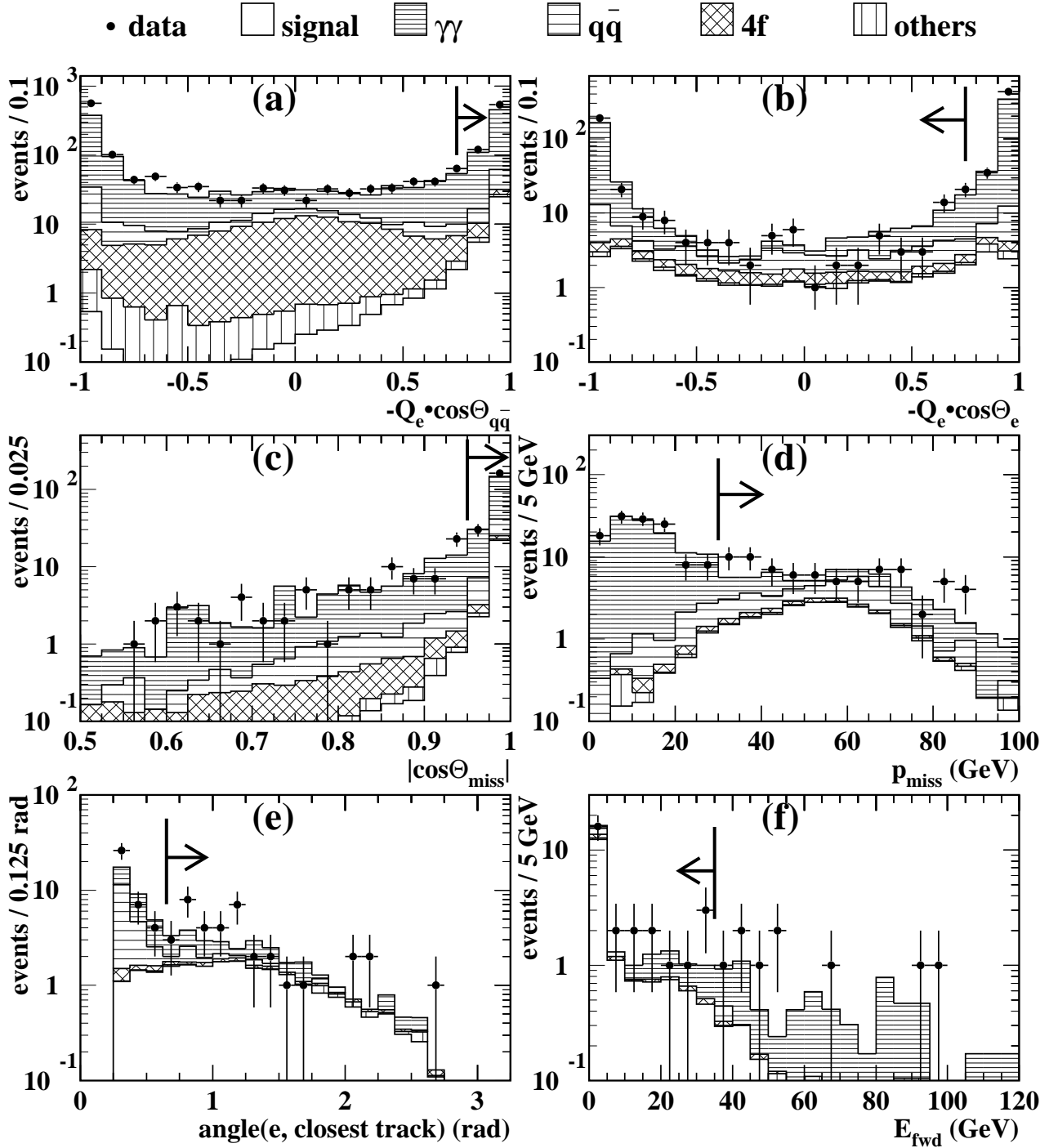


Figure 3: Distributions of the selection variables. The histograms show the various Monte Carlo simulations and the points are the data. The arrows point into the selected regions. The cuts have been applied successively. Only statistical errors are shown.

# OPAL

• data

□ signal

▨ background

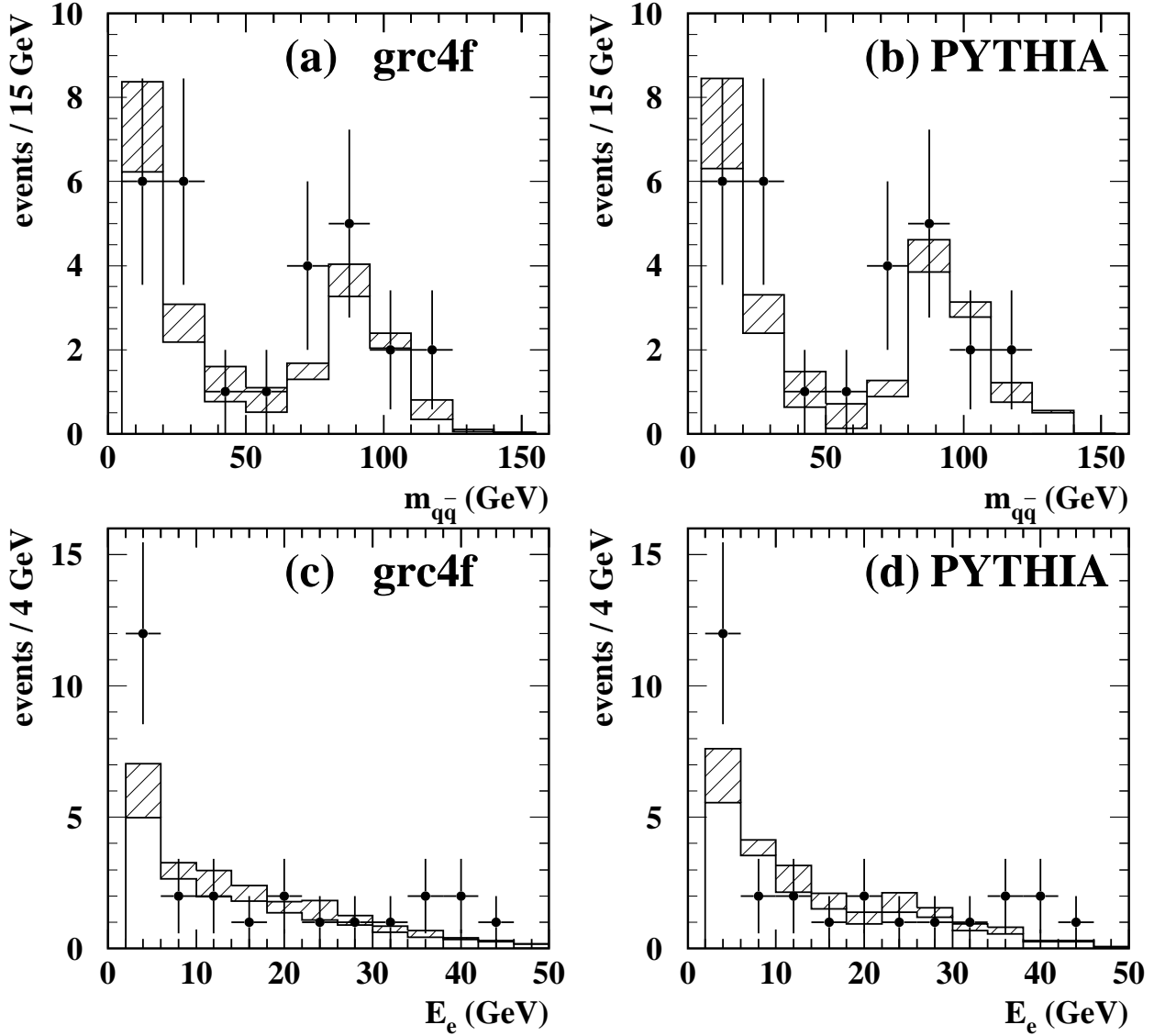


Figure 4: Distributions of  $m_{q\bar{q}}$  and  $E_e$  after all cuts. In Figures (a) and (c) the signal is simulated using the *grc4f* generator. In (b) and (d) we have used *PYTHIA* instead of *grc4f*. The histograms show the various Monte Carlo simulations and the points are the data. Only statistical errors are shown.

# OPAL

• data

□ signal

▨ background

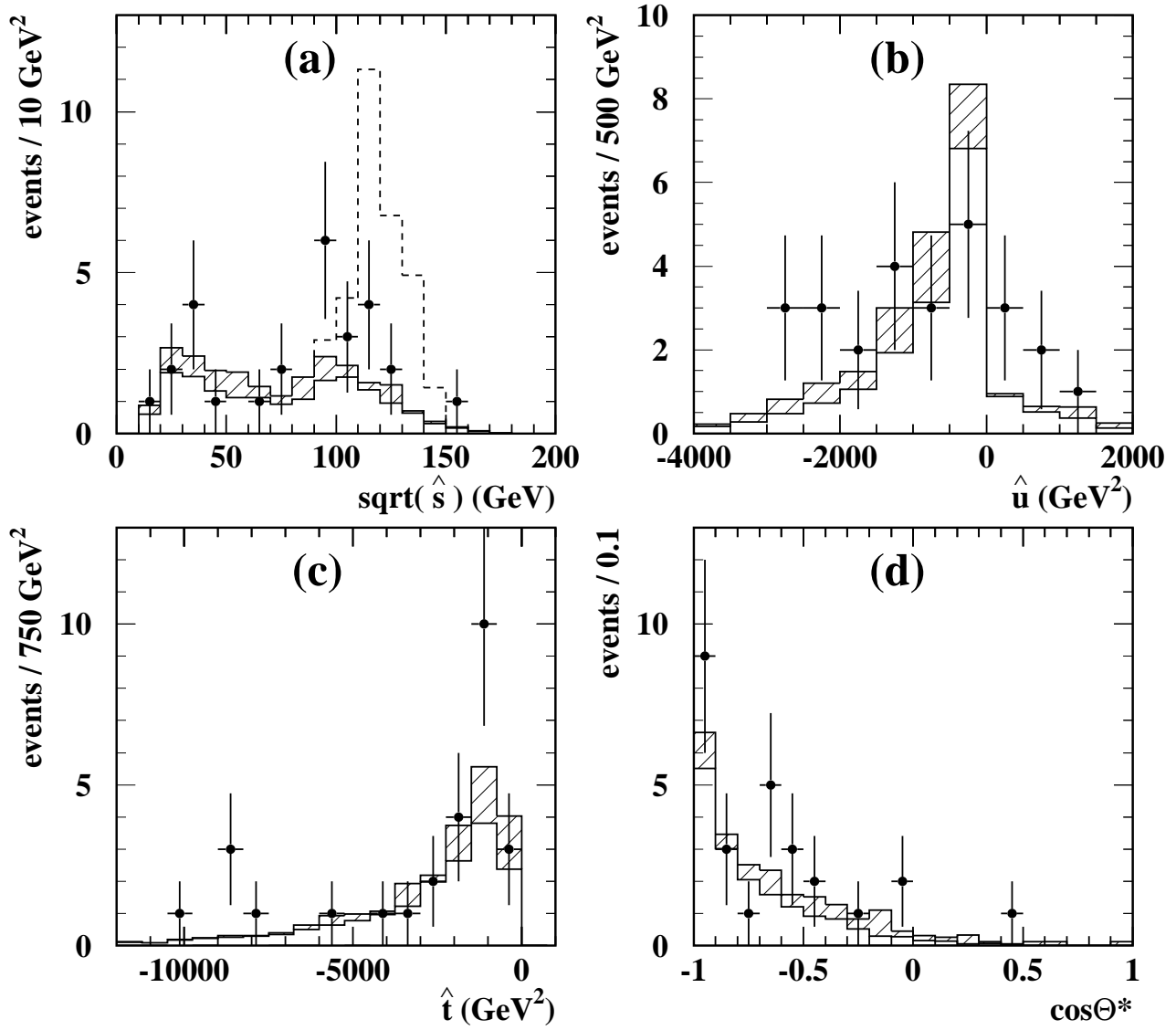


Figure 5: Distributions of  $(\hat{s})^{1/2}$ ,  $\hat{t}$ ,  $\hat{u}$  and  $\cos\theta^*$  after all cuts. The histograms show the various Monte Carlo simulations and the points are the data. The dashed histogram in (a) is a hypothetical  $e^*$  signal, as described in the text. Only statistical errors are shown.